

Supporting Information

A novel strategy for encapsulating metal sulfide nanoparticles inside hollow carbon nanospheres-aggregated microspheres for efficient potassium ion storage

Jin-Sung Park^{1,†}, Soo Young Yang^{1,†}, Jung-Kul Lee^{2,*}, and Yun Chan Kang^{1,*}

¹Department of Materials Science and Engineering, Korea University, Anam-Dong, Seongbuk-Gu, Seoul 136-713, Republic of Korea

²Department of Chemical Engineering, Konkuk University, Hwayang-dong, Gwangjin-gu, Seoul 143-701, Republic of Korea

[†] These two authors contributed equally to this work.

*Corresponding authors. E-mail address: yckang@korea.ac.kr (Yun Chan Kang), jkrhee@konkuk.ac.kr (Jung-Kul Lee)

Supplementary Material Characterization

The morphological traits of HCA-FeS and FeS microspheres were analyzed using field-emission scanning electron microscopy (FE-SEM; Hitachi, S-4800) and transmission electron microscopy (FE-TEM; JEOL, JM-2100F). The oxidation states and chemical bonding present in the samples were examined by X-ray photoelectron spectroscopy (XPS; Thermo Scientific K-Alpha™) using focused monochromatic Al K_{α} radiation. The crystallographic characteristics of the samples were analyzed by X-ray diffraction (XRD; X-Pert PRO with Cu K_{α} radiation) at the Korea Basic Science Institute (Daegu). The carbon contents of the samples were determined by thermogravimetric (TG, Pyris 1 Thermogravimetric Analyzer, Perkin Elmer) analysis conducted in the temperature range of 25–800 °C at a ramping speed of 10 °C min^{-1} in air. The structure of carbon in the powder was investigated using Raman spectroscopy (Jobin Yvon LabRam HR800, excitation source: 632.8 nm He/Ne laser). The specific surface area and pore structure of the obtained samples were characterized by Brunauer-Emmett-Teller (BET) method using N_2 gas as the adsorbate. *Ex situ* TEM and XPS analyses were performed using the same apparatus for the fully discharged and charged states.

Supplementary Electrochemical Characterization

The electrochemical properties of HCA-FeS and FeS microspheres were analyzed using 2032-type coin cells assembled in an Ar-filled glove box. The anode was prepared using a slurry process; the active material, carbon black (Super P), and sodium carboxymethyl cellulose (CMC) binder were mixed in a weight ratio of 7:2:1 using water in a mortar. The slurry was applied onto a Cu foil with a doctor blade and dried in a vacuum oven. The diameter and the average mass loading of the electrode were 1.4 cm and 1.2 mg cm^{-2} , respectively. Potassium metal and microporous polypropylene film were used as the counter electrode and the separator, respectively. The electrolyte was 1 M potassium bis(fluorosulfonyl) imide (KFSI) dissolved in a mixture of ethylene carbonate and diethyl carbonate (EC/DEC, volumetric ratio of 1:1). The fabricated cells were galvanostatically discharged and charged in the voltage range of 0.001–3.0 V at various current densities. Cyclic voltammetry (CV) curves were obtained at sweep rates from 0.1 to 2.0 mV s^{-1} . *In situ* and *ex situ* electrochemical impedance spectroscopy (EIS) were performed in the frequency range of 0.01 Hz and 100 kHz.

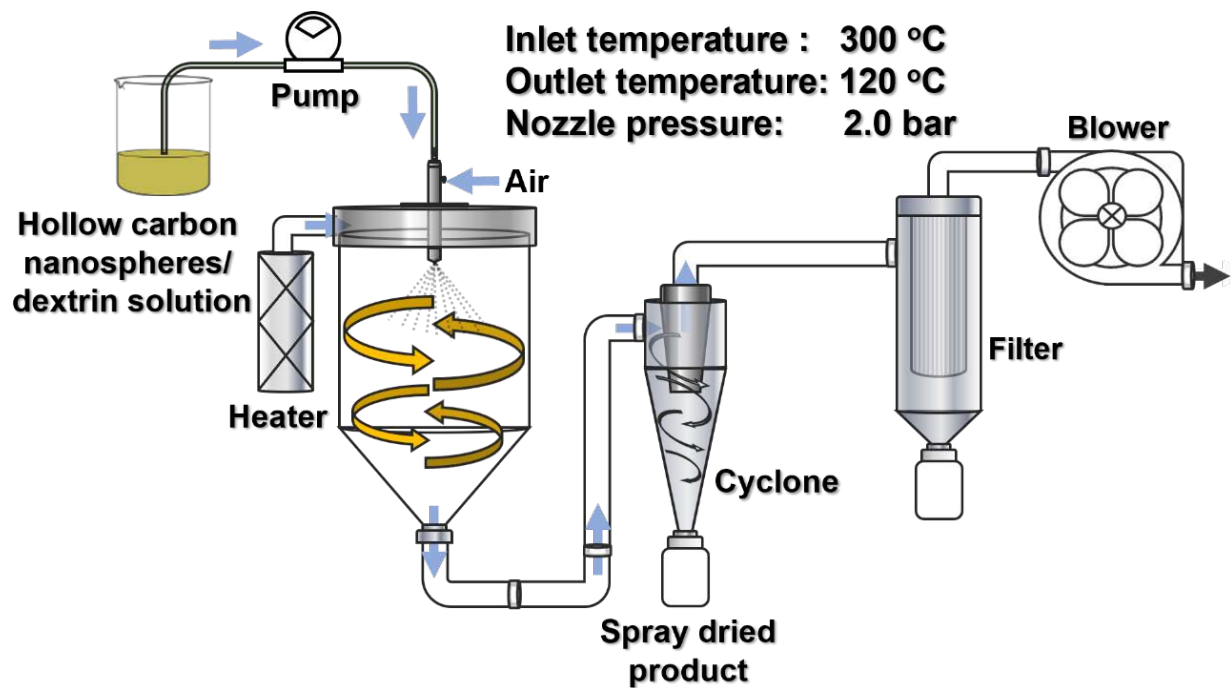


Fig. S1. Schematic illustration of the spray drying apparatus.

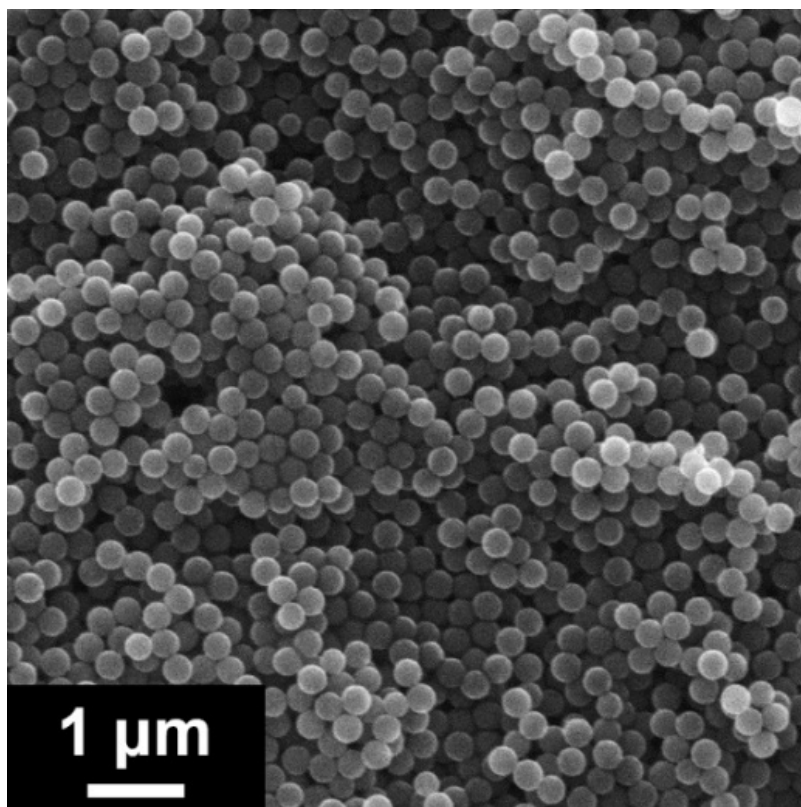


Fig. S2. SEM image of SiO₂@RF nanospheres.

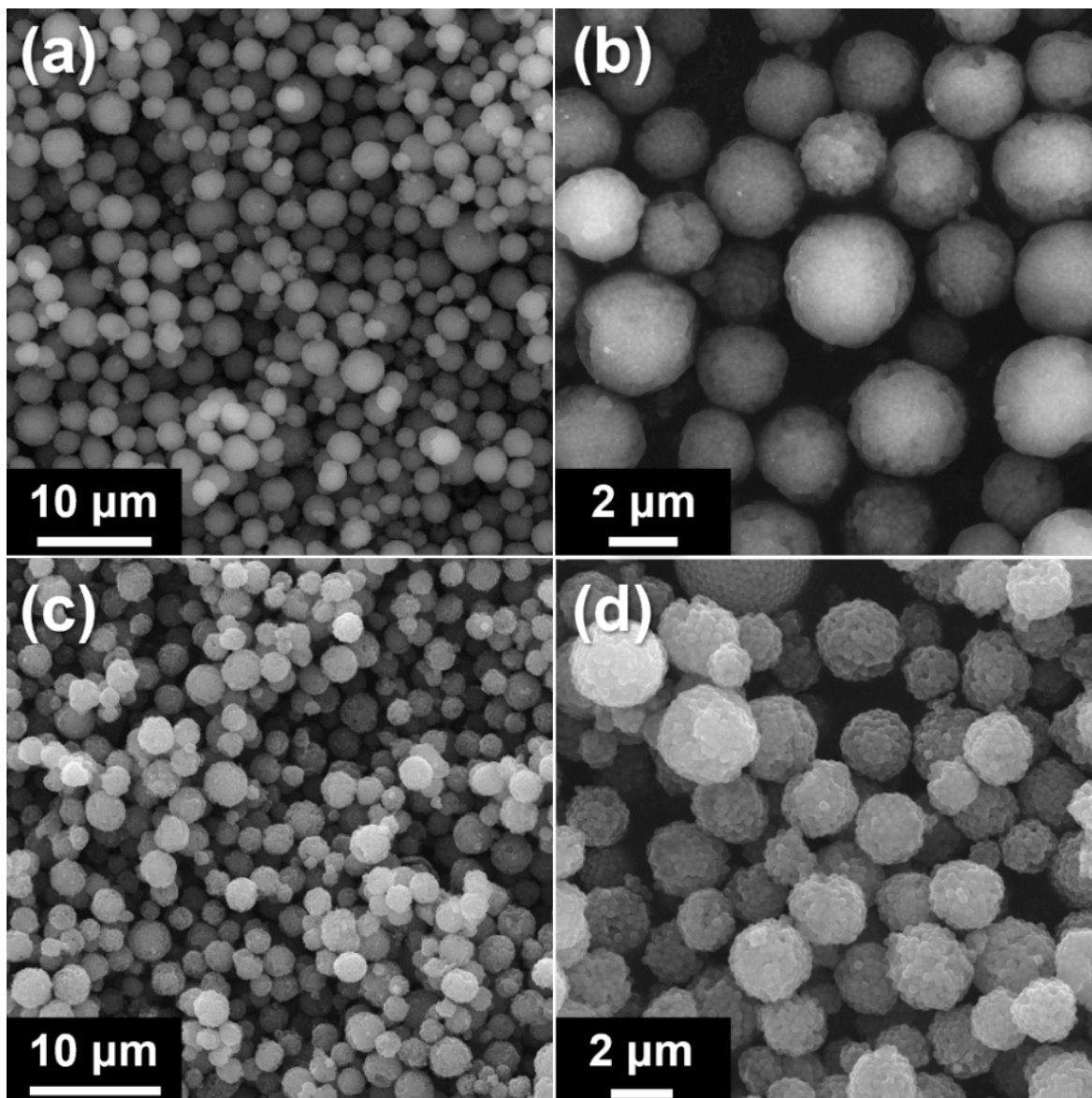


Fig. S3. SEM image of nanospheres-aggregated microspheres obtained from spray drying of $\text{SiO}_2\text{@RF}$ nanospheres (a,b) before and (c,d) after heat treatment under Ar atmosphere.

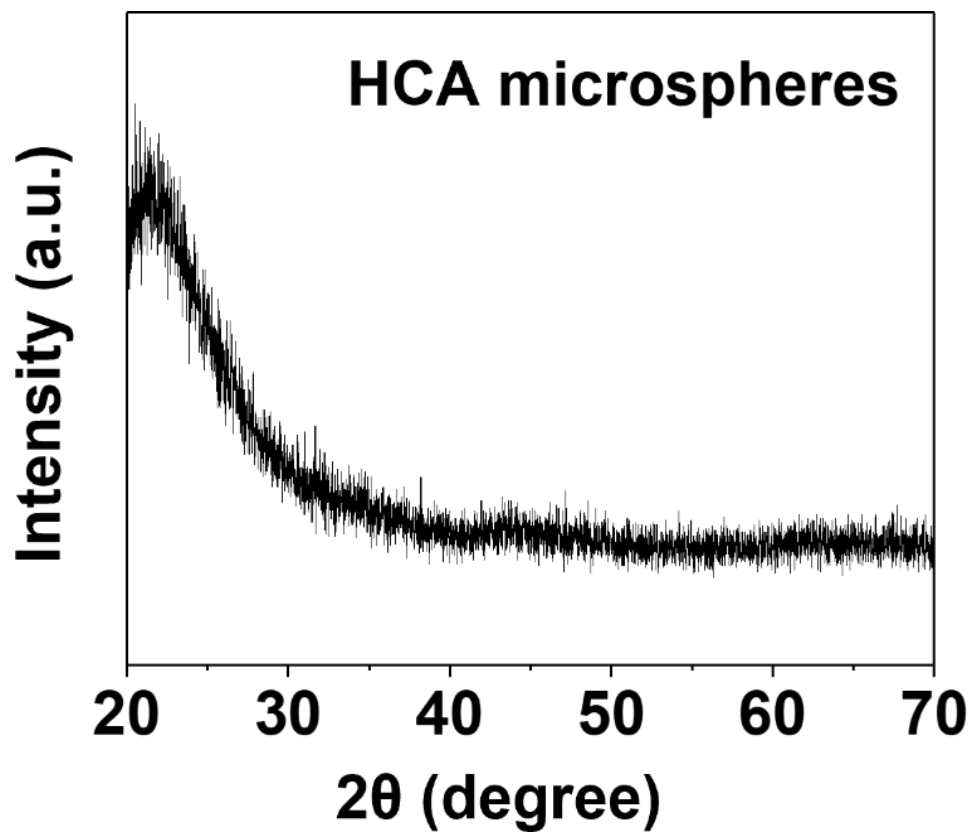


Fig. S4. XRD pattern of HCA microspheres.

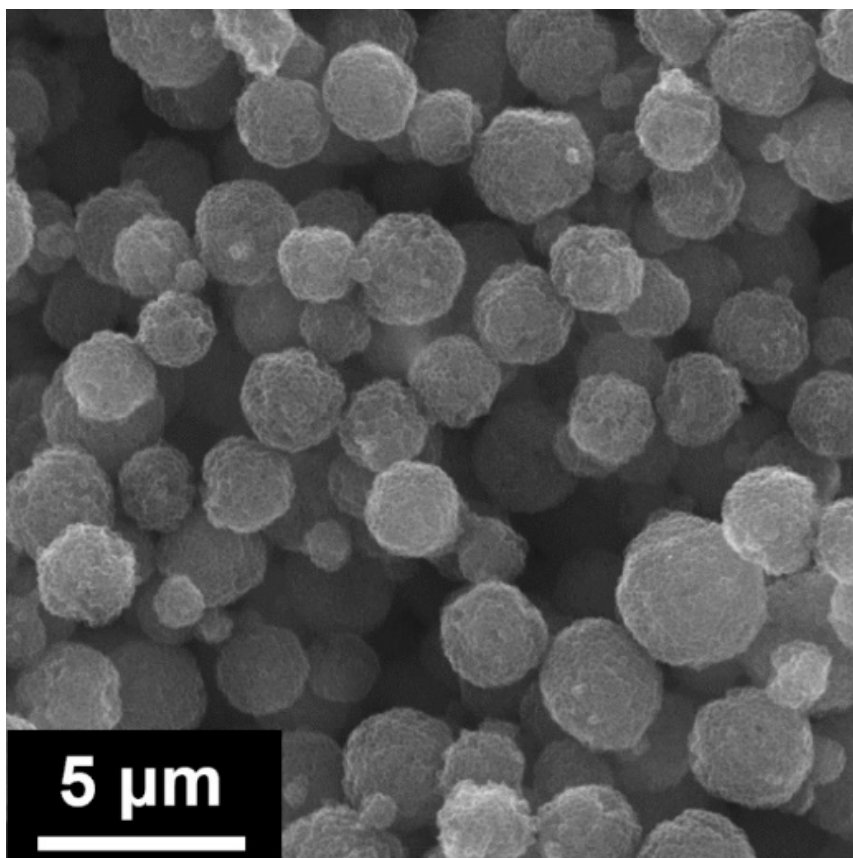


Fig. S5. SEM image of HCA microspheres obtained from aqueous solution with dextrin after iron nitrate infiltration.

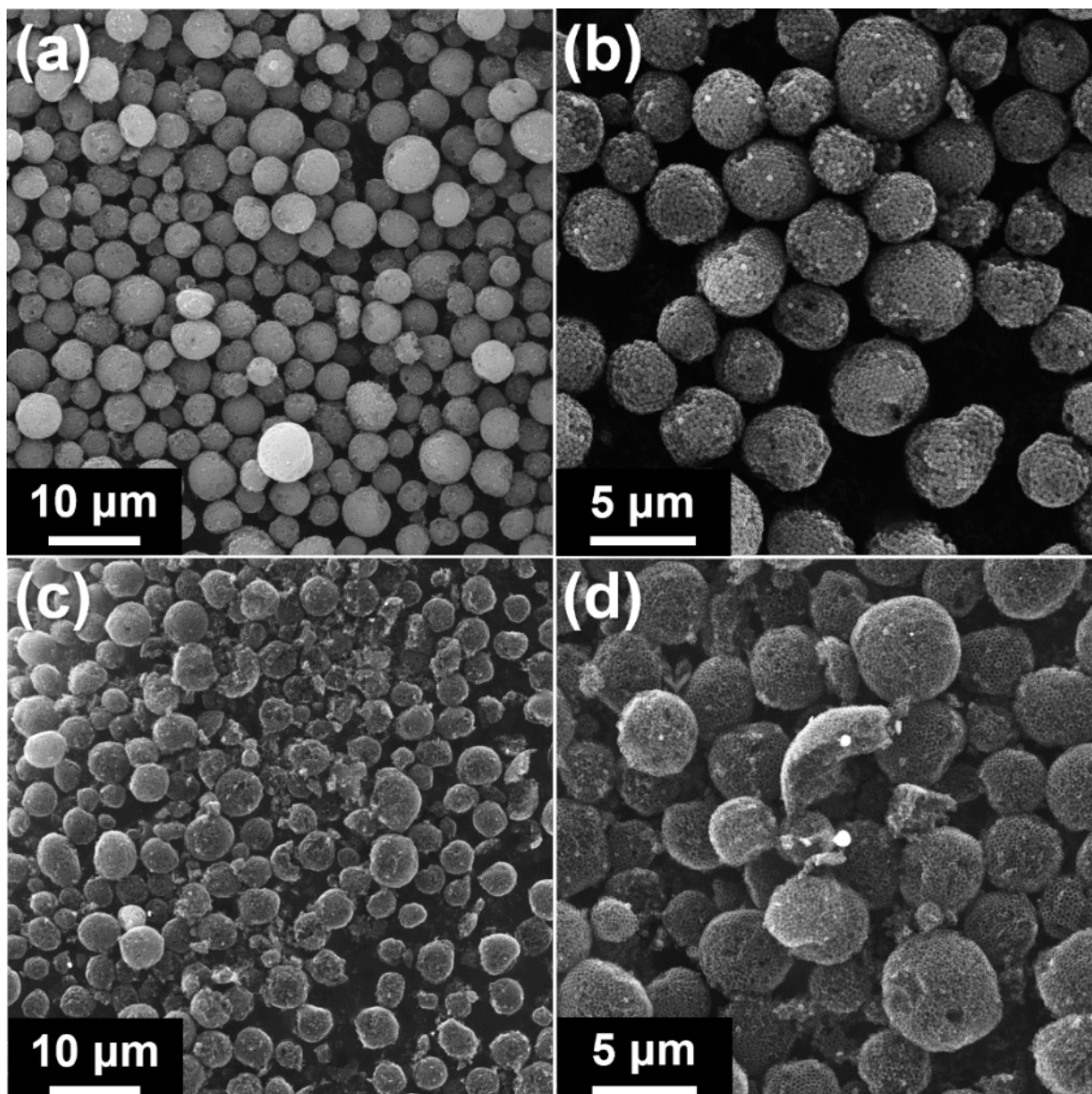


Fig. S6. SEM image of hollow carbon aggregate microspheres obtained from aqueous solution without dextrin and subsequent carbonization: (a,b) Before and (c,d) after NaOH etching.

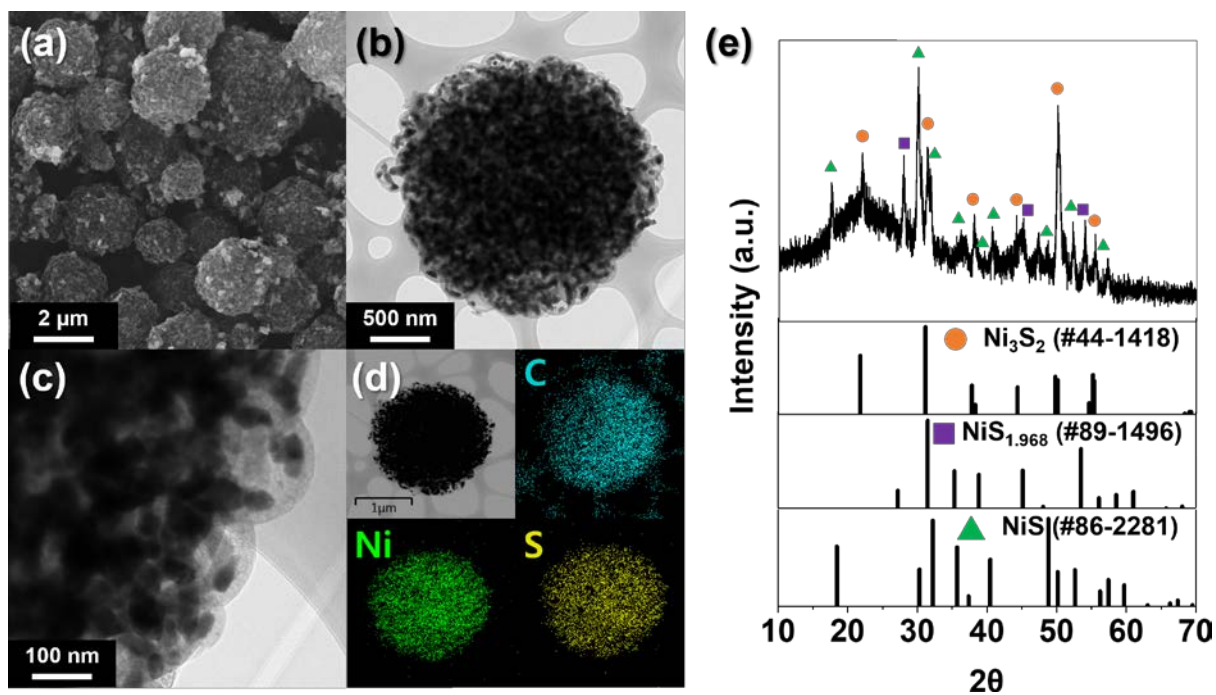


Fig. S7. (a) SEM, (b,c) TEM images, (d) elemental dot mapping images, and (e) XRD pattern of hollow carbon aggregate microspheres containing nickel sulfide materials prepared from an identical method using nickel nitrate salt.

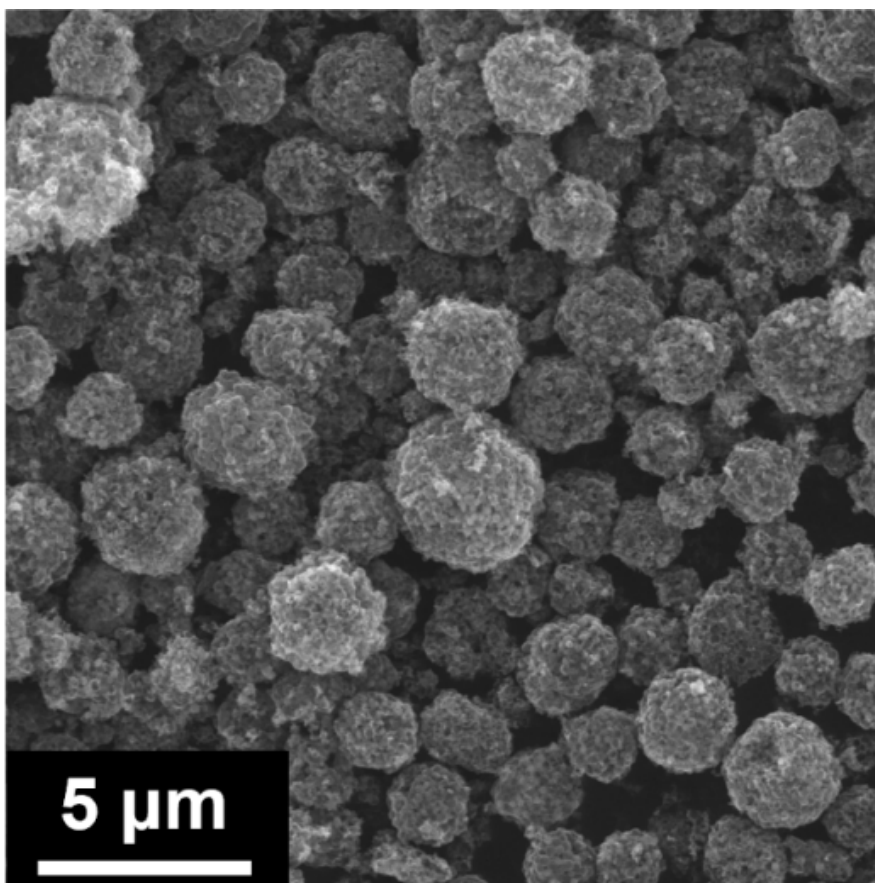


Fig. S8. SEM image of Fe₂O₃ microspheres obtained from oxidation of iron nitrate-infiltrated HCA microspheres at 350 °C for 5 h.

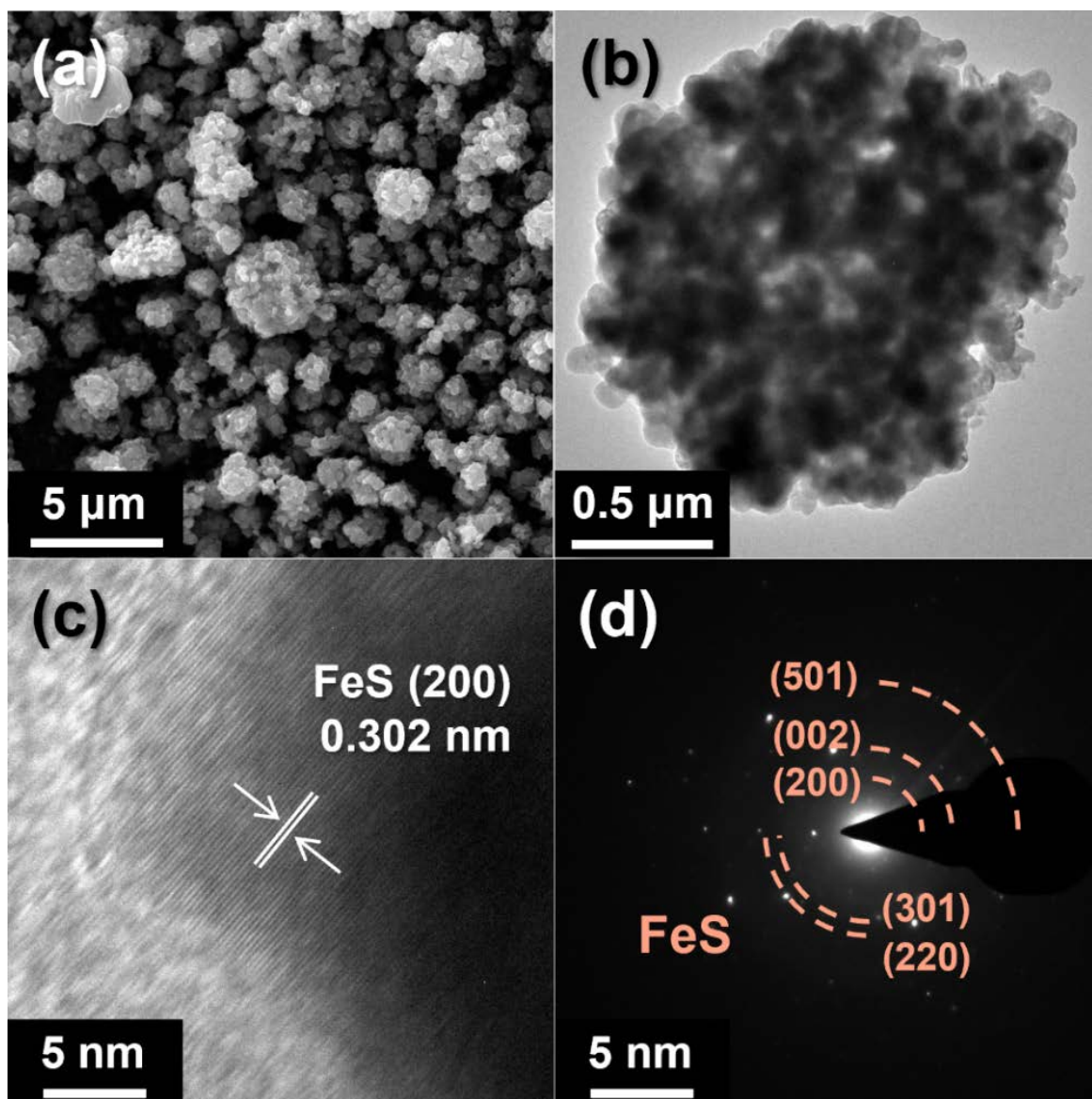


Fig. S9. (a) SEM, (b) TEM, (c) HR-TEM images, and (d) SAED pattern of FeS microspheres.

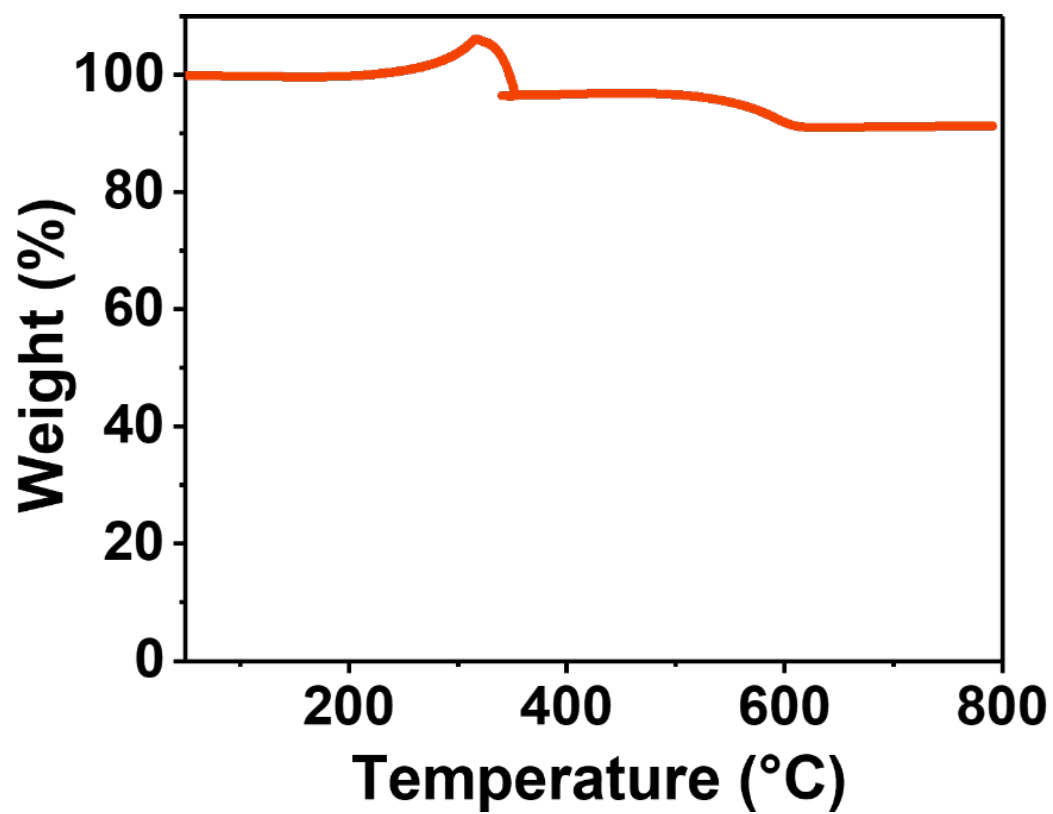


Fig. S10. TGA curve of FeS microspheres.

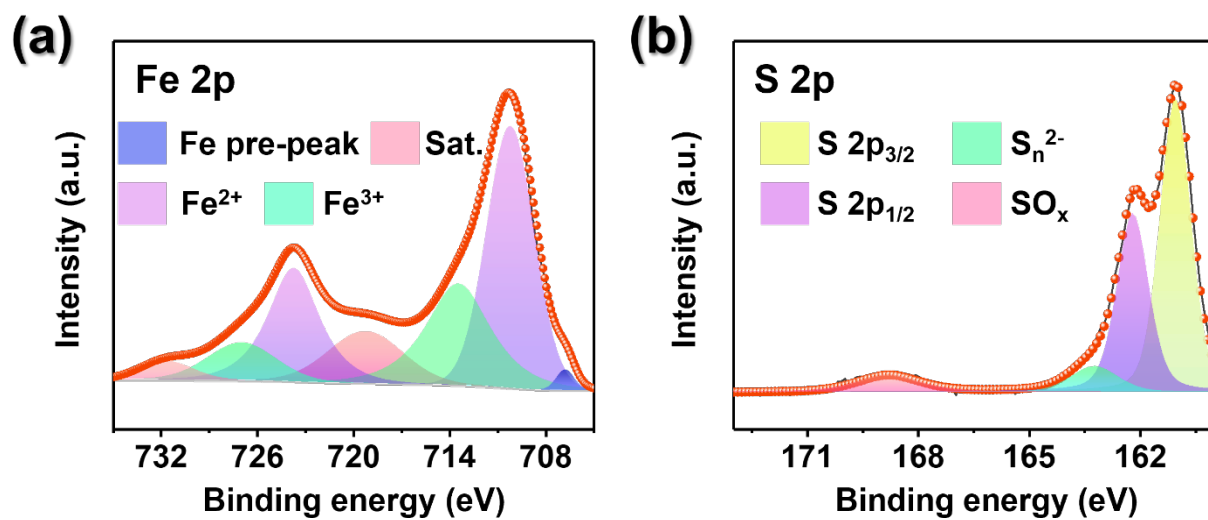


Fig. S11. XPS spectra of FeS microspheres: (a) Fe 2p and (b) S 2p spectra.

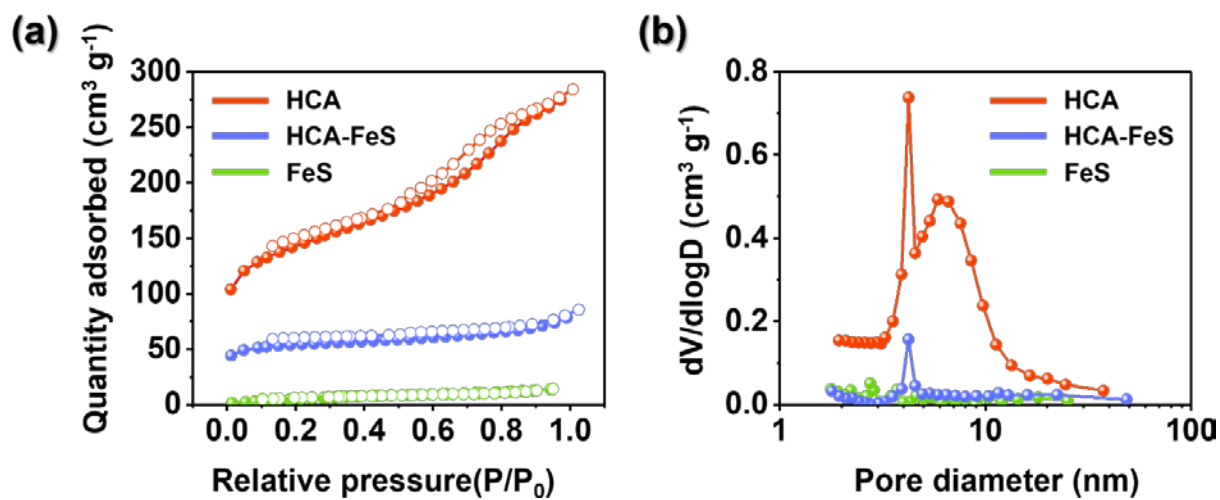
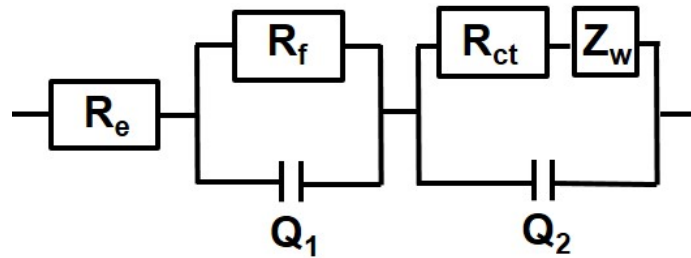


Fig. S12. (a) N_2 adsorption and desorption isotherms and (b) BJH pore size distributions of HCA microspheres, HCA-FeS microspheres, and FeS microspheres.

Equivalent circuit model



R_e : the electrolyte resistance, corresponding to the intercept of high frequency semicircle at Z_{re} axis

R_f : the SEI layer resistance corresponding to the high-frequency semicircle

Q_1 : the dielectric relaxation capacitance corresponding to the high-frequency semicircle

R_{ct} : charge transfer resistance related to the middle-frequency semicircle

Q_2 : associated double-layer capacitance related to the middle-frequency semicircle

Z_w : K-ion diffusion resistance

Fig. S13. Randles-type equivalent circuit used to deconvolute Nyquist plots.

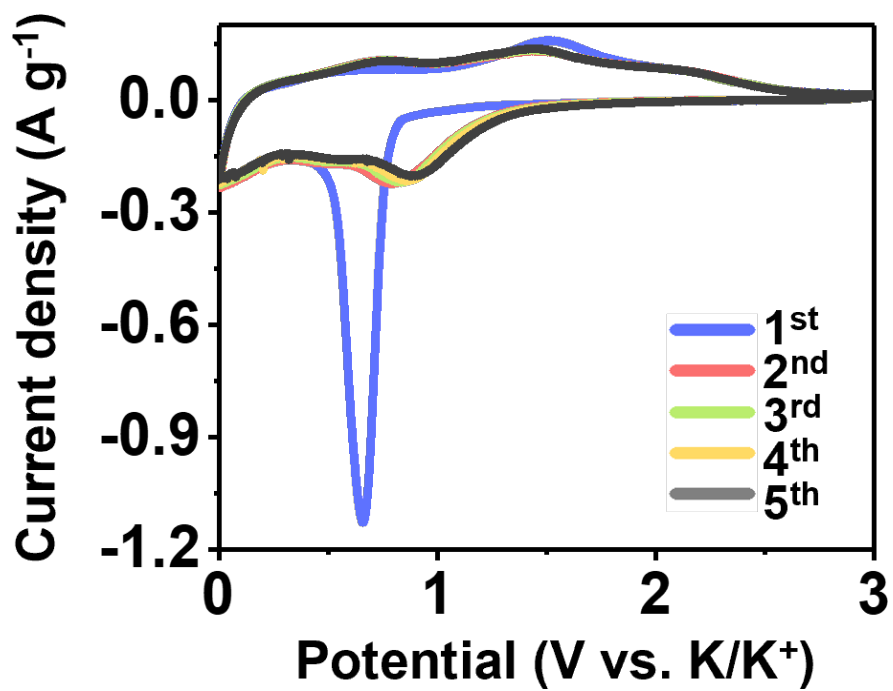


Fig. S14. CV curves of FeS microspheres.

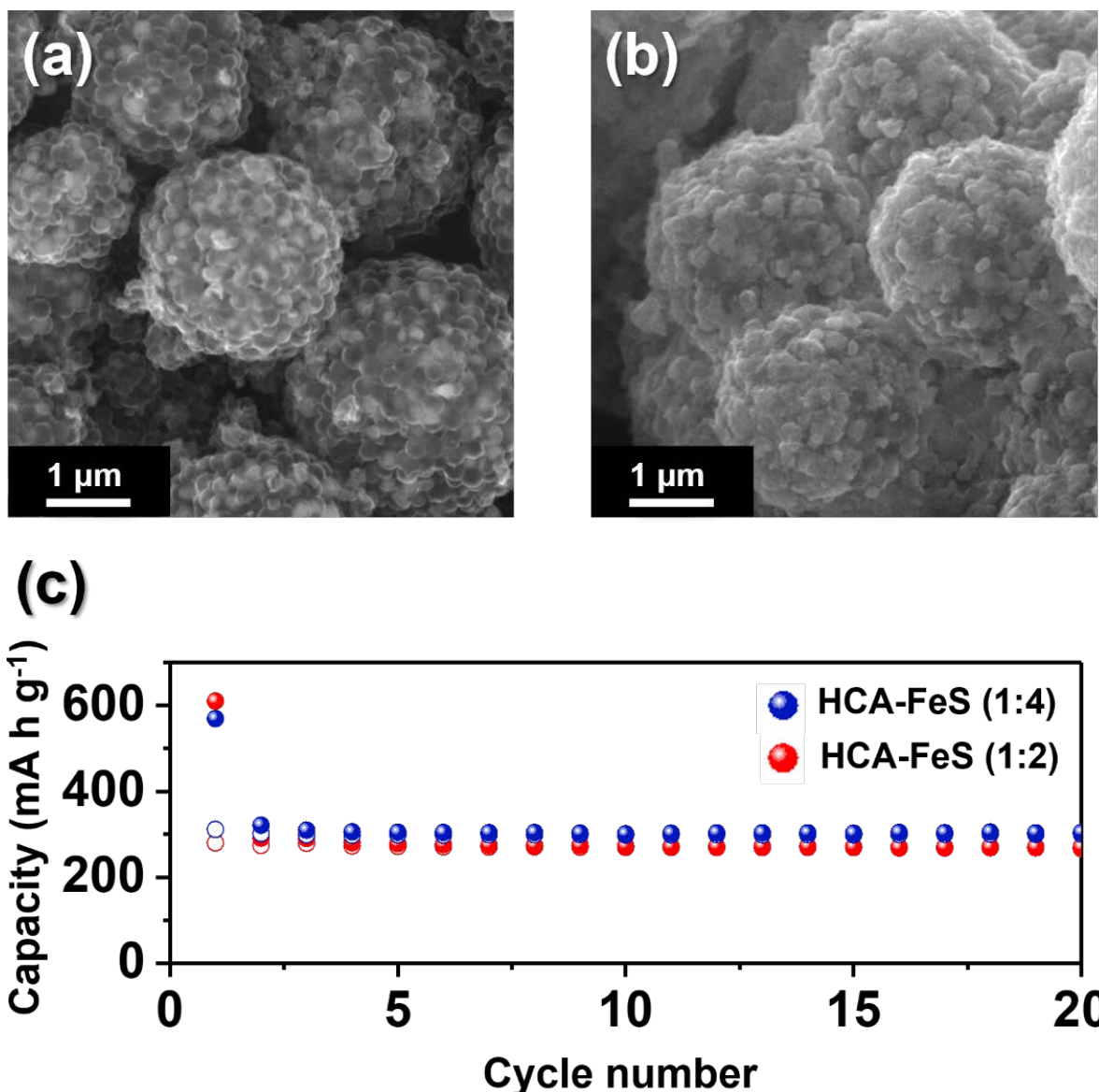


Fig. S15. SEM images of (a) HCA-FeS (1:2) and (b) HCA-FeS (1:4) microspheres, and (c) cycle performances at 0.1 A g⁻¹.

Since the contents of Fe_{1-x}S may have a great influence on the potassium storage performance, the content of Fe_{1-x}S incorporated into HCA microspheres was controlled. Originally, 0.06 g iron nitrate was infiltrated into 0.02 g HCA microspheres, which corresponds to a weight ratio of 3:1. For comparison, 0.04 g and 0.08 g iron nitrate were infiltrated into 0.02 g HCA, which corresponds to weight ratio of 2:1 and 4:1, respectively. HCA-FeS microspheres prepared with 2:1 and 4:1 iron nitrate to HCA microspheres are denoted as HCA-FeS (1:2) and HCA-FeS (1:4) microspheres, respectively. The SEM images of HCA-FeS (1:2) and HCA-FeS (1:4) microspheres are shown in Fig. S15. SEM image of HCA-FeS (1:2) microspheres in Fig. S15a

reveals that FeS nanoparticles are well encapsulated within the HCA microspheres. In contrast, HCA-FeS (1:4) microspheres revealed that aggregation occurred between the microspheres. This can be attributed to the large amount of iron nitrate, which may have filled the pores of HCA, resulting in iron nitrate salt located at the surface. During the sulfidation process, the iron nitrate salts underwent sintering process, which resulted in the aggregation between the microspheres. The potassium storage performances of HCA-FeS (1:2) and HCA-FeS (1:4) microspheres were also tested and shown in Fig. S15c. Since the ratio of FeS particles with relatively high capacity and HCA microspheres with lower capacity is low in case of HCA-FeS (1:2), the electrode exhibited lower capacity of 291 mA h g⁻¹ at 0.1 A g⁻¹. HCA-FeS (1:4) microspheres exhibited capacities of 321 mA h g⁻¹ at 0.1 A g⁻¹, which revealed that the optimum ratio of HCA-FeS is 1:3.

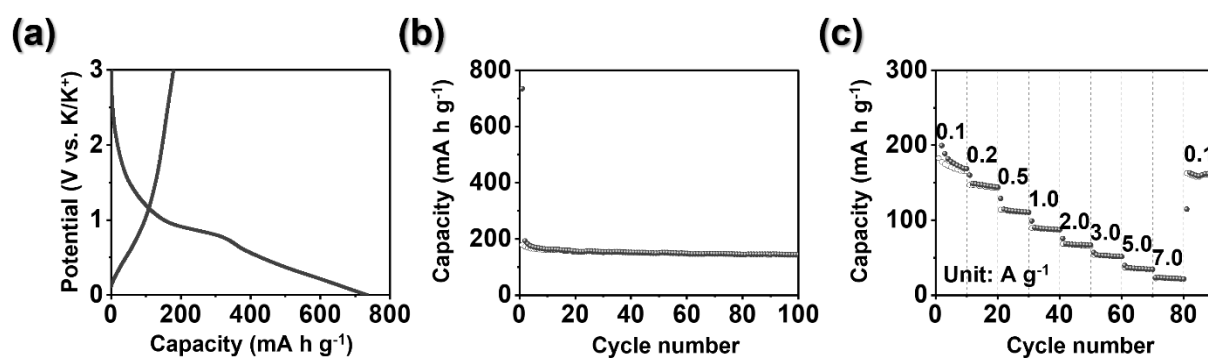


Fig. S16. Electrochemical properties of HCA microspheres as anode for potassium ion battery: (a) initial charge-discharge profiles, (b) cycle performance, and (c) rate capability.

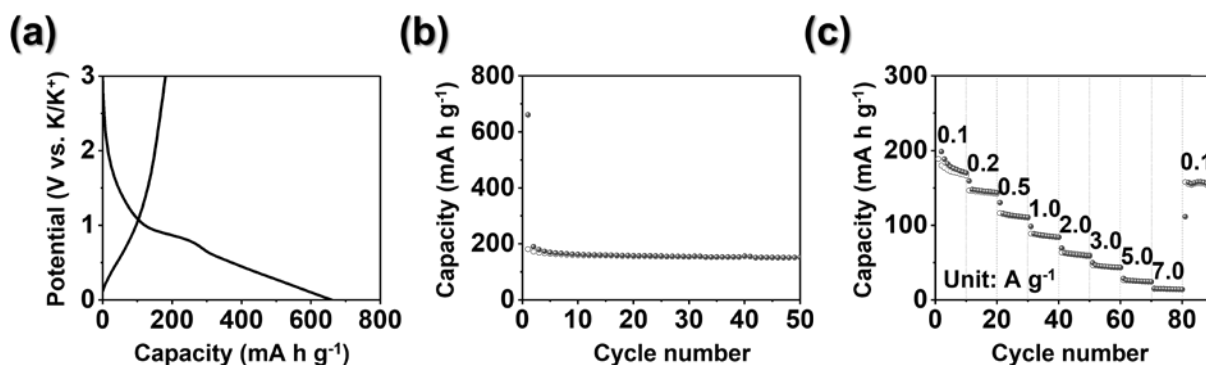


Fig. S17. Electrochemical properties of S-incorporated HCA microspheres as anode for potassium ion battery: (a) initial charge-discharge profiles, (b) cycle performance, and (c) rate capability.

To demonstrate whether incorporation of sulfur atoms into carbon has a positive effect on the electrochemical performance or not, a control sample was prepared from sulfidation of HCA microspheres in the presence of thiourea at 400 °C under 10% H₂/Ar gas flow. The electrochemical properties of the prepared anode are shown Fig. S17; not much improvement in potassium ion storage performance was observed in comparison to that of HCA microspheres (Fig. S16).

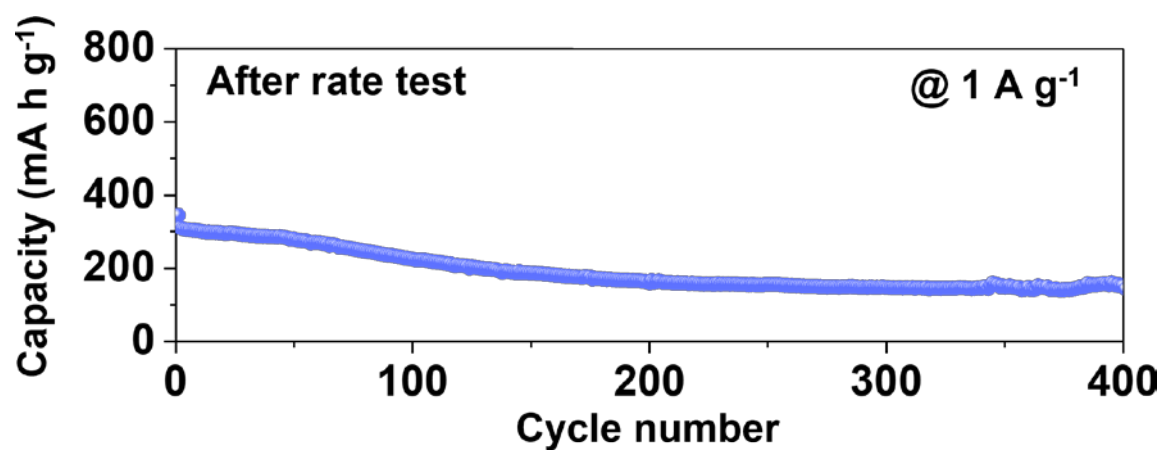


Fig. S18. Cycle performance of HCA-FeS microspheres at 1.0 A g⁻¹ tested right after rate capability test.

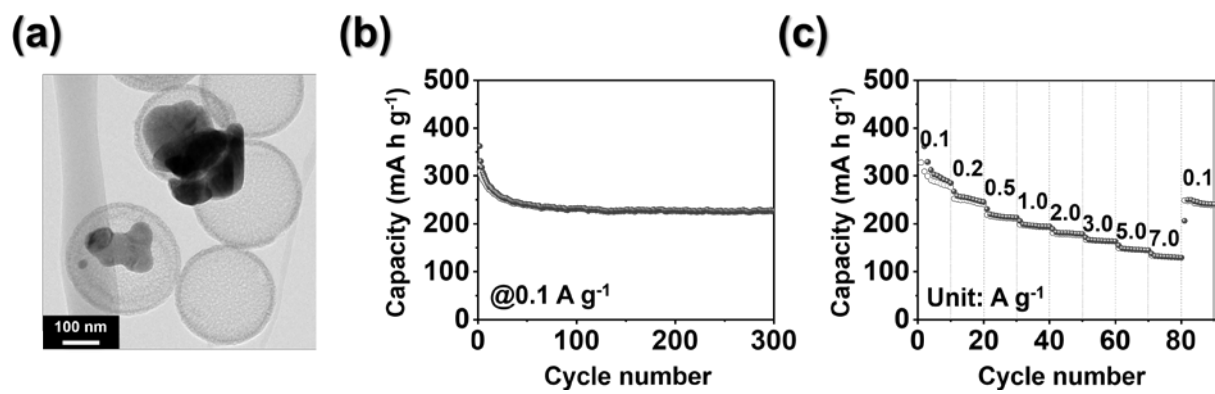


Fig. S19. (a) TEM image, (b) cycle performance at 0.1 A g⁻¹, and (c) rate capability of HC-FeS.

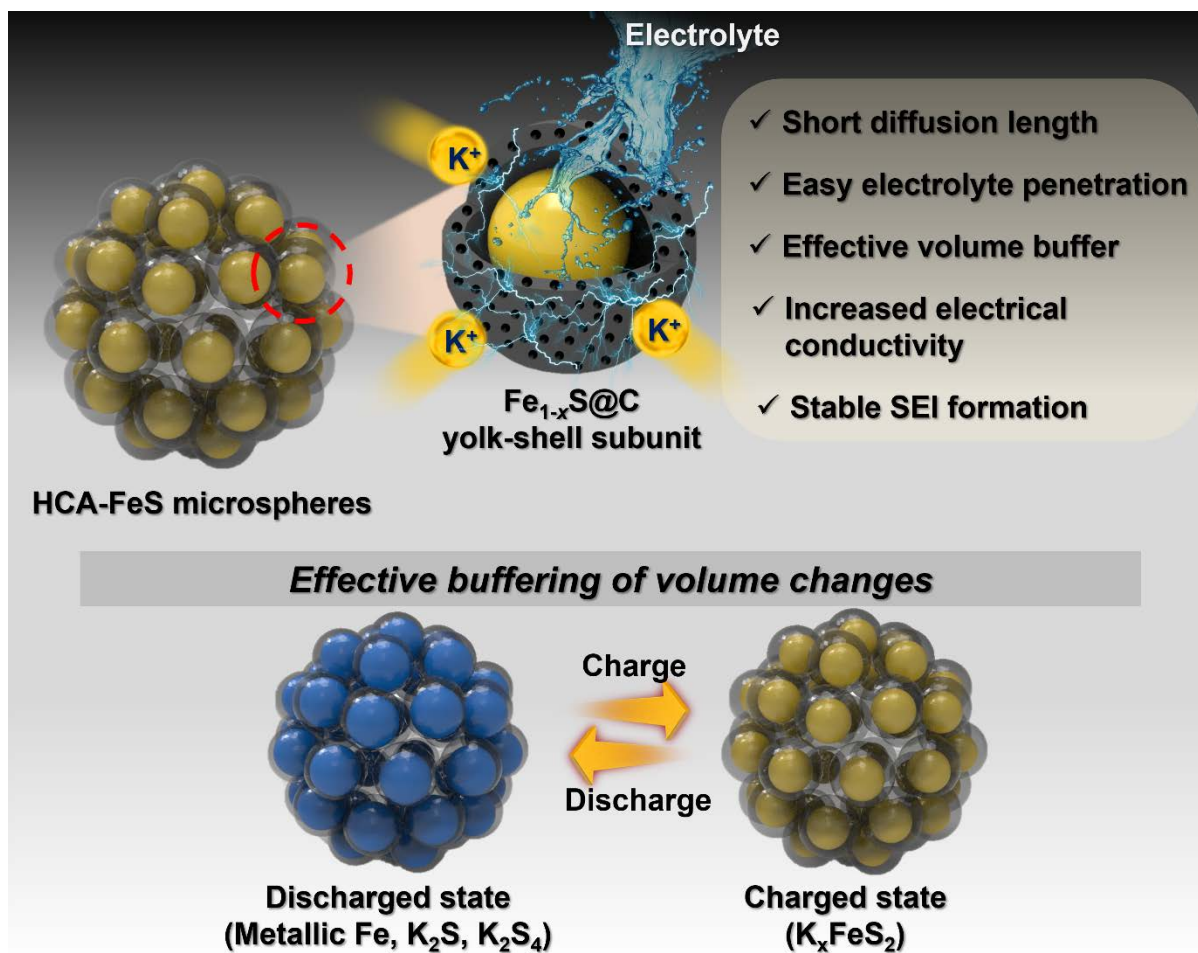


Fig. S20. Schematic illustration of the numerous merits using HCA-FeS microspheres as anode for PIBs.

Table S1. Electrochemical properties of iron sulfide materials applied as anode for potassium ion batteries.

Electrode materials	Preparation method	Current density [A g ⁻¹]	Initial discharge/charge capacities [mA h g ⁻¹]	Discharge capacity [mA h g ⁻¹] and (cycle number)	Rate capability [mA h g ⁻¹]	Ref.
G@Y-S FeS ₂ @C	Solution process	0.3	1357/489	270(1000)	166 (15 A g ⁻¹)	[26]
Crystal-like Fe _{1-x} S	Solvothermal	0.1	562.3/361.8	420.8(100) at 0.1 A g ⁻¹ 212.9(250) at 1.0 A g ⁻¹	167.6 (5 A g ⁻¹)	[53]
Fe _{1-x} S/S-doped carbon nanosheet	Hydrothermal	0.05	784/~489	430(300)	170 (2 A g ⁻¹)	[S1]
Fe _{1-x} S microcube	Solvothermal	0.05	622/432	418(60)	123 (6 A g ⁻¹)	[S2]
Fe _{1-x} S/SWNT@C	Hydrothermal method	0.1	1116/678	472(50)	172 (20 A g ⁻¹)	[S3]
FeS@SPC	Calcination	0.1	868.6/450.0	309(100)	140 (5 A g ⁻¹)	[S4]
Yolk shell structured FeS@C	Spray drying	0.5	595.4/358.5	256.5(100)	113.8 (5 A g ⁻¹)	[S5]
FeS ₂ @rGO	Freeze drying	0.5	563/333	123(420)	151 (0.5 A g ⁻¹)	[S6]
Yolk-shell FeS ₂ @C	Solvothermal	1	~986/451	295(150)	182 (10 A g ⁻¹)	[S7]
FeS ₂ @G@CNF (FeS ₂ @graphene @carbon nanofibers)	Electrospinning	1	~626/394	120(680)	171 (1 A g ⁻¹)	[S8]
HCA-FeS microspheres	Spray drying	0.1	703/371	401(200)	180 (7 A g ⁻¹)	<i>This work</i>

References

- S1. Y. Xu, B. Wang, H. Wu, R. Ti, and Z. Chen, *Mater. Lett.* 2021, **291**, 129419.
- S2. Y. Xu, F. Bahmani, and R. Wei, *Microsyst. Nanoeng.* 2020, **6**, No. 75.
- S3. Y. Zhao, X. Shi, S. J. H. Ong, Q. Yao, B. Chen, K. Hou, C. Liu, Z. J. Xu, and L. Guan, *ACS Nano* 2020, **14**, 4463-4474.
- S4. Z. Yan, J. Liu, H. Wei, X. Yang, Y. Yao, Z. Huang, H. Li, Y. Kuang, J. Ma, and H. Zhou, *J. Colloid Interface Sci.* 2021, **593**, 408-416.
- S5. J. H. Kim, G. D. Park, and Y. C. Kang, *Int. J. Energy Res.* 2021, **45**, 14910-14919.
- S6. J. Xie, Y. Zhu, N. Zhuang, H. Lei, W. Zhu, Y. Fu, M. S. Javed, J. Li, and W. Mai, *Nanoscale* 2018, **10**, 17092-17098.
- S7. Z. Zhao, Z. Hu, R. Jiao, Z. Tang, P. Dong, Y. Li, S. Li, and H. Li, *Energy Storage Mater.* 2019, **22**, 228.
- S8. C. Chen, Y. Yang, X. Tang, R. Qiu, S. Wang, G. Cao, and M. Zhang, *Small* 2019, **15**, 1804740.

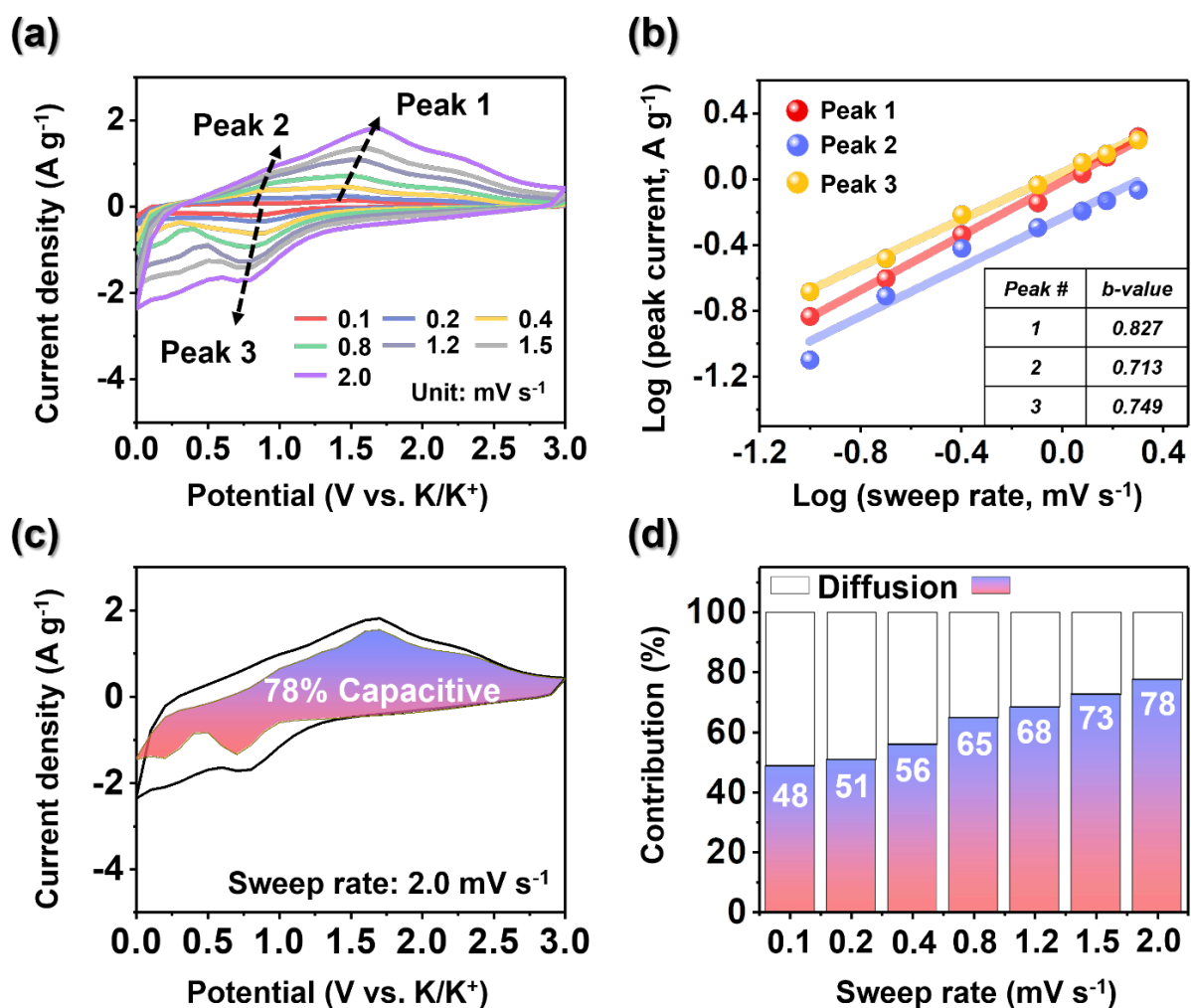


Fig. S21. Analysis on the electrochemical kinetics of FeS microspheres: (a) CV curves obtained at various sweep rates, (b) linear fitted $\log(\text{peak current})$ vs. $\log(\text{sweep rate})$ for Peaks 1~3, (c) CV curves that show the capacitive contribution (colored area) in comparison to the total current (at 2.0 mV s^{-1}), and (d) capacity contributions obtained at various sweep rates.

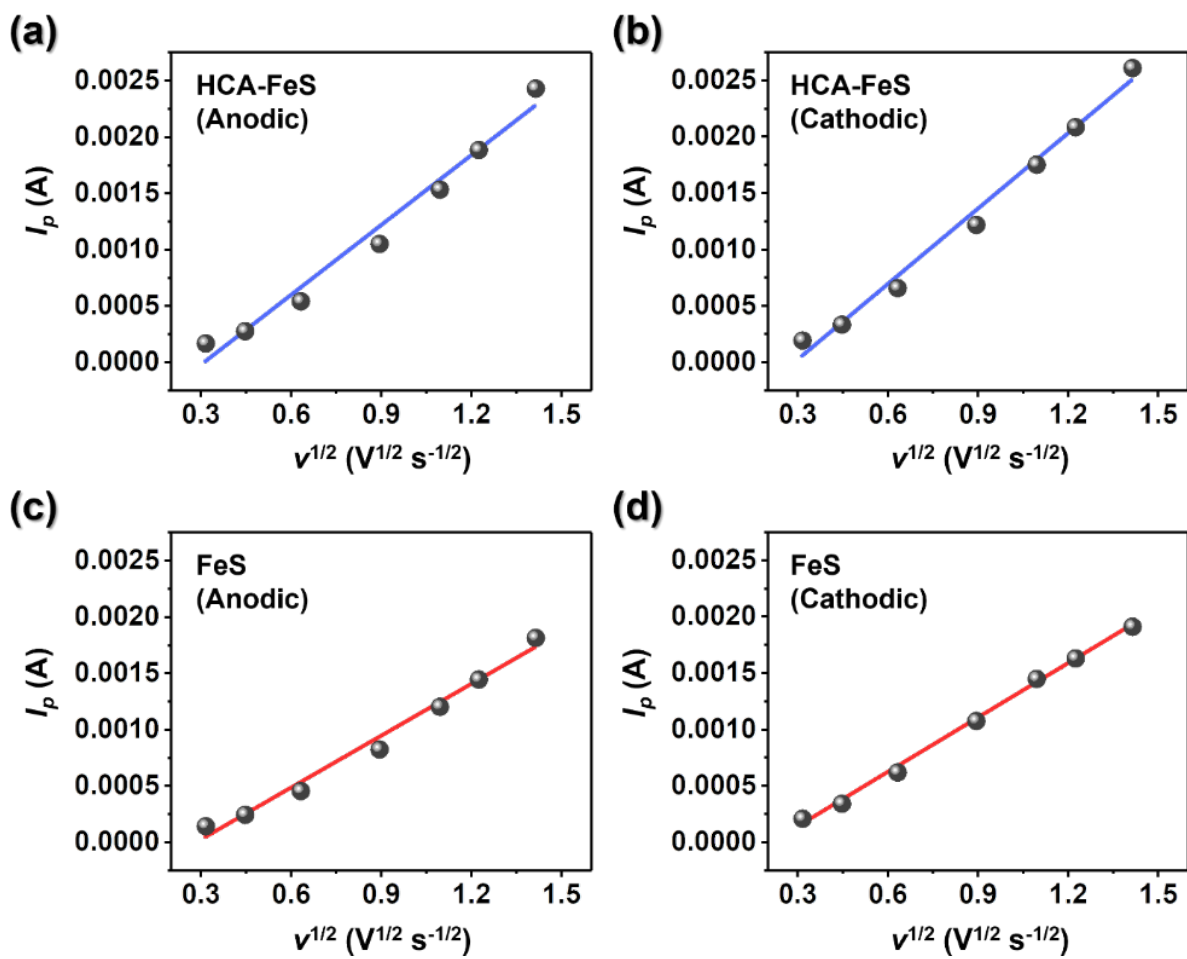


Fig. S22. Relationship between peak current (I_p) vs. square root of sweep rates ($v^{1/2}$) for (a,b) HCA-FeS and (c,d) FeS microspheres.

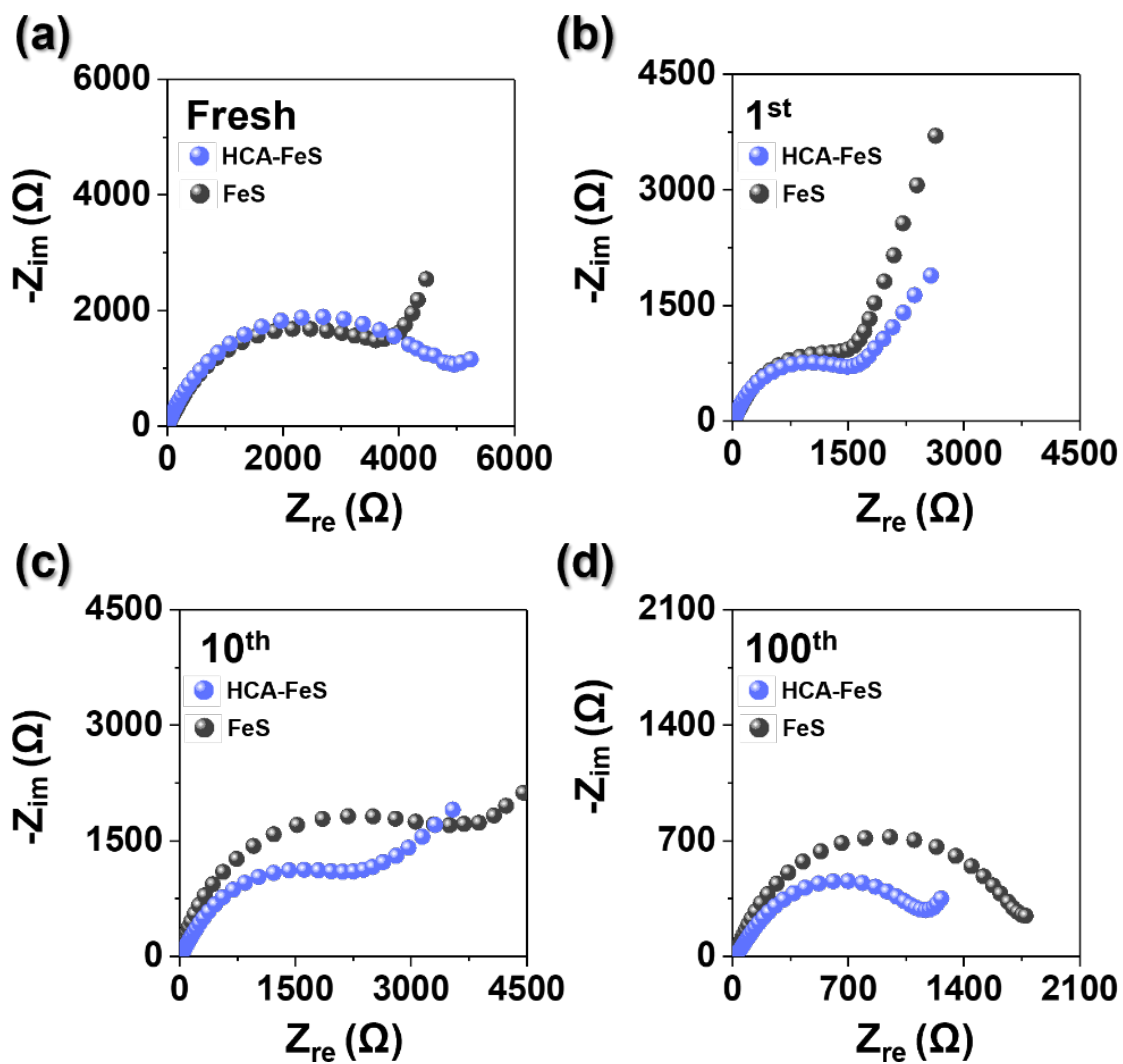


Fig. S23. *Ex situ* Nyquist plots of HCA-FeS and FeS microspheres.

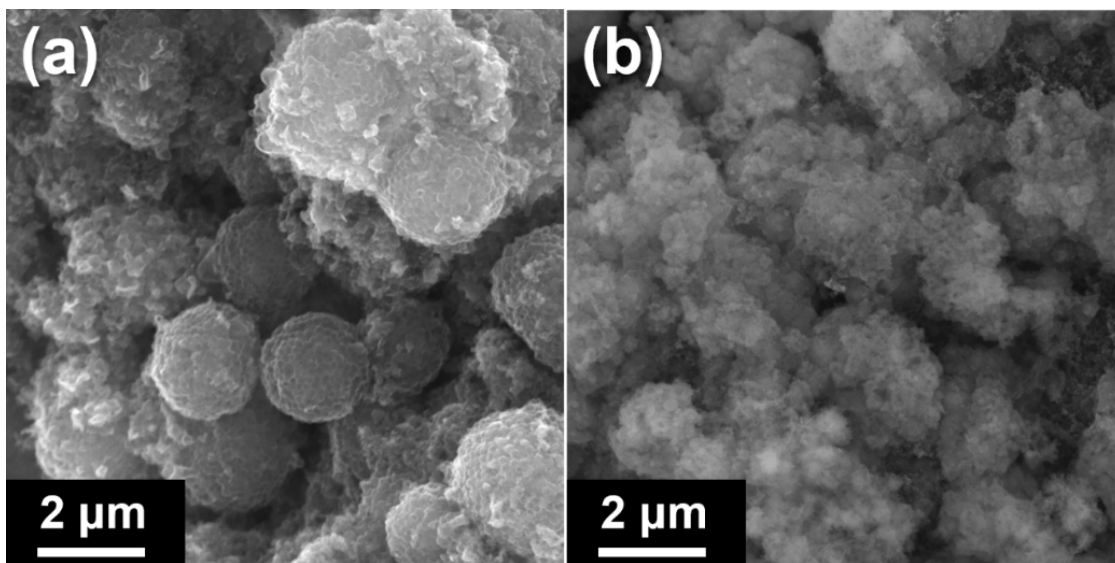


Fig. S24. SEM images of (a) HCA-FeS and (b) FeS microspheres after 100 cycles.